


Spin-Orbit Coupling in Single-Layer Ferrimagnets: Direct Observation of Spin-Orbit Torques and Chiral Spin Textures

Sachin Krishnia^{1,*}, Eloi Haltz^{1,†}, Léo Berges¹, Lucia Aballe², Michael Foerster,² Laura Bocher¹, Raphaël Weil¹, André Thiaville¹, João Sampaio^{1,†} and Alexandra Mougin¹

¹Université Paris-Saclay, CNRS, Laboratoire de Physique des Solides, 91405 Orsay, France

²Alba Synchrotron Light Facility, CELLS, Barcelona E-08290, Spain

 (Received 15 July 2020; revised 25 July 2021; accepted 3 August 2021; published 24 August 2021)

We demonstrate that the effects of spin-orbit coupling and inversion asymmetry exist in a single Gd-Fe-Co ferrimagnetic layer, even without a heavy-metal interface. We use electric transport measurements to quantify the spin-orbit torques. We measure the Dzyaloshinskii-Moriya interaction using the Brillouin light-scattering measurement technique, and we observe the resulting chiral magnetic textures using x-ray photoemission electron microscopy. We attribute these effects to a composition variation along the thickness that we observe by scanning transmission electron microscopy. We show that these effects can be optimized by varying the Gd-Fe-Co thickness or in combination with interfacial effects.

DOI: [10.1103/PhysRevApplied.16.024040](https://doi.org/10.1103/PhysRevApplied.16.024040)

I. INTRODUCTION

Magnetic layers interfaced with materials with strong spin-orbit coupling (SOC), such as Pt and Ta, manifest several fascinating phenomena when the inversion symmetry is broken [1–4]. One direct consequence of SOC is the interplay between charge and spin transport *via* the spin Hall effect (SHE) in heavy metals (HMs), which leads to nonequilibrium spin accumulation at the surfaces [5,6]. Another mechanism, the Rashba effect, arises when electrical carriers move in an interfacial electric field and experience the resultant magnetic field that couples with their spins [7,8]. Both mechanisms give rise to spin-orbit torques (SOTs) in the adjacent magnetic layer, with dampinglike and fieldlike components [9–11]. Surprisingly, SOTs are detected in a single layer of Ni-Fe, even in the absence of HM adjacent layers [12,13]. Moreover, SOTs are an efficient way to manipulate chiral magnetic textures, such as Néel domain walls (DWs) [2,3] and skyrmions [14], the chirality of which is induced by another product of SOC, the Dzyaloshinskii-Moriya interaction (DMI) [1].

Recently, the combination of SOTs and DMI has enabled fast and efficient magnetization dynamics in rare-earth (RE)–transition-metal (TM) ferrimagnetic films interfaced with a HM [15–17]. In conventional 3d-TM/HM

bilayers, Pt 5d (or Pd 4d) states hybridize strongly with the 3d states of the TM, leading to proximity effects and an enhanced orbital moment [8,18]. In RE-TM alloys, spintronic effects are described by the combination of localized 4f magnetism and itinerant magnetism of the *s-p-d* band structure [19]. It was shown earlier that itinerant magnetism in these materials was dominated by RE 5d and TM 3d states [18]. This hybridization implies that RE atoms with unpaired 5d electrons may exhibit a large SOC [20–22], suggesting that SOT and the DMI can appear, even in the absence of an adjacent HM layer. Very recent observations of interfacial DMI in Tm- and Tb-based oxide garnets are attributed to the orbital moment of the RE [23,24]. Furthermore, an interface-independent DMI originating in the bulk of a Gd-Fe-Co ferrimagnet layer has been reported using indirect methods based on asymmetric magnetic reversal [25], which was attributed to broken symmetry caused by inhomogeneity of the RE atoms along the film thickness. On the other hand, experiments on (Co/Tb)_n multilayers do not show any SOT contribution from the RE [26]. The underlying origin of SOC and the role of the RE on SOC in ferrimagnets, hence, remain to be understood and need to be addressed by direct experimental evidence.

Here, we provide direct evidence of the internal SOC effects in single-layer Gd-Fe-Co ferrimagnets. The SOC-induced effects, such as SOTs, DMI, and chiral magnetic textures, are observed in a Gd-Fe-Co film without any HM layer, but with a symmetry-breaking inhomogeneous Gd concentration along the thickness, a key ingredient to observe the SOC effects.

*sachinbudana@gmail.com

†joao.sampaio@universite-paris-saclay.fr

‡S. Krishnia and E. Haltz contributed equally to this work.

II. FILM DEPOSITION AND CHARACTERIZATION

Gd_{0.35}(Fe₈₅Co₁₅)_{0.65} 5-nm-thick films are deposited on thermally oxidized Si substrates by *e*-beam coevaporation of Gd and Fe-Co targets under ultrahigh vacuum ($\sim 10^{-10}$ mbar) [27]. Al (5 nm) and Pt (7 nm) capping layers are deposited to prevent oxidation of the ferrimagnets. The Pt-capped sample is used as a reference and, hereafter, Gd-Fe-Co refers to the Al-capped sample, unless mentioned otherwise. The Gd-Fe-Co film is composed of two sublattices of Gd (RE) and Fe-Co (TM) coupled antiferromagnetically [28]. Magnetization as a function of temperature is shown in Fig. 1(a). At the magnetic compensation temperature, $T_M \approx 275$ K for this sample, the net magnetization vanishes and the coercive field diverges [Fig. 1(b)].

To measure the Hall effect, the films are patterned into 5- μ m-wide Hall cross structures using *e*-beam lithography and a hard-mask etching technique. Figures 1(c) and 1(d) show hysteresis loops obtained by the anomalous Hall effect (AHE) below and above T_M . The electrical properties are dominated by the TM sublattice and, therefore, the change in sign of the Hall resistance (R_{AHE}) across T_M is a signature of the reversal of the alignment of the Fe-Co sublattice with the external field, as shown in the insets. The effective anisotropy field [H_k ; Fig. 1(b) in

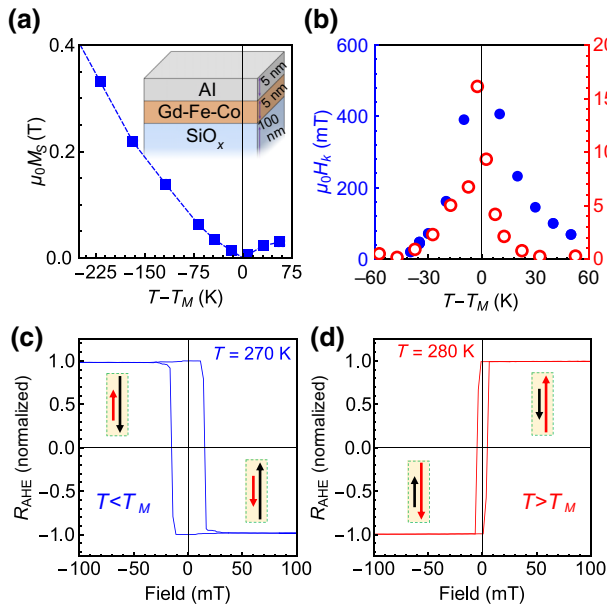


FIG. 1. (a) Net magnetization (M_s) versus temperature measured using superconducting quantum interference device (SQUID) magnetometry. (b) Anisotropy field (H_k) in blue and coercive field (H_c) in red as a function of temperature, which diverge at T_M . Normalized R_{AHE} vs perpendicular magnetic field at (c) $T = 270$ K $< T_M$ and (d) $T = 280$ K $> T_M$. Arrows represent the direction and relative magnitude of Gd (black) and Fe-Co (red) magnetic moments.

blue], obtained by fitting R_{AHE} versus in-plane field [29], diverges at T_M . The spin-flop transitions are not observed over the measured temperature and magnetic field ranges (see the Supplemental Material [30]).

III. CURRENT-INDUCED TORQUES

To investigate the existence of SOC inside the ferrimagnetic layer, we quantify the two components of current-induced torques by using the second-harmonic Hall voltage measurement technique [9,31]. The measurement geometries are shown in Figs. 2(a) and 2(b). This technique uses an ac current of low frequency ($f = 1.33$ kHz) to induce periodic magnetization oscillations, which modulate R_{AHE} at frequency f and the anomalous Hall voltage at frequency $2f$. By measuring simultaneously the first and second harmonics as a function of in-plane field (H) applied along or transversely to the current direction [$H \parallel I_{\text{ac}}$ and $H \perp I_{\text{ac}}$, Figs. 2(a) and 2(b)], we extract the dampinglike (H_{DL}) or fieldlike (H_{FL}) effective fields (see

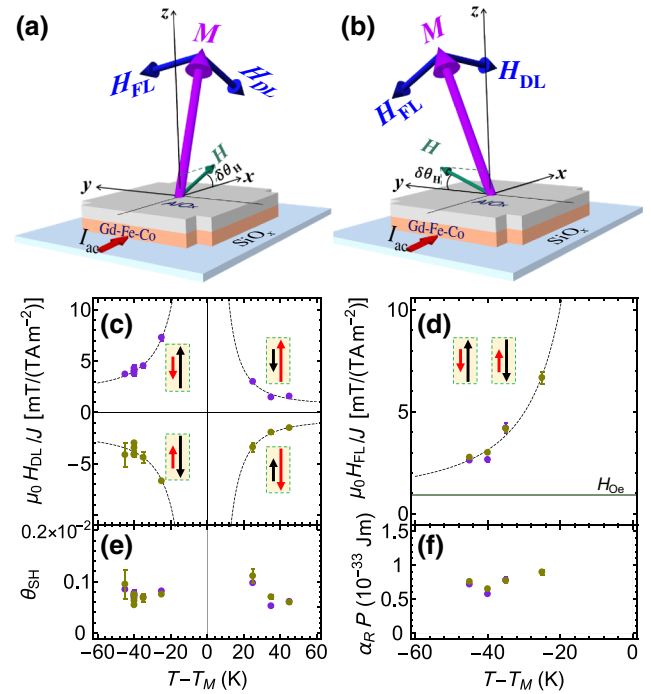


FIG. 2. Illustration of harmonic Hall measurements in (a) longitudinal and (b) transverse geometries to obtain H_{DL} and H_{FL} . H and I_{ac} are the applied magnetic field and ac current, respectively. (c) H_{DL}/J (with J estimated in the Gd-Fe-Co layer) and (d) H_{FL}/J vs temperature. Purple (khaki) points correspond to an up (down) saturated state. Diagrams represent the direction and magnitude of Gd (black) and Fe-Co (red) magnetic moments. Dotted lines are guides to the eye. Estimated Oersted field (~ 1 mT/TA m⁻²) due to I_{ac} is shown by a line. (e) Spin Hall angle (θ_{SH}) and (f) Rashba parameter ($\alpha_R P$) vs temperature.

the Supplemental Material [30]). To increase the sensitivity, the analysis method is improved to include magnetic fields larger than H_k .

Figure 2(c) shows the temperature dependence of H_{DL} per current density (H_{DL}/J). At a given temperature, H_{DL} increases linearly with current (showing that the thermally induced Hall voltage is negligible; see the Supplemental Material [30]) and changes sign when the magnetization is reversed, in agreement with the expected symmetry of SHE-induced torque, $\mathbf{H}_{DL} = H_{DL}(\hat{\mathbf{m}} \times \hat{\sigma})$, where $\hat{\mathbf{m}}$ and $\hat{\sigma}$ are the unit vectors along magnetization and spin-polarization directions [32]. Assuming that the SHE is the main source of H_{DL} , we expect

$$\mu_0 H_{DL} = \frac{\hbar}{2e} \frac{1}{M_s t} J \theta_{SH},$$

where θ_{SH} is the spin Hall angle and should be temperature-independent for a given material. H_{DL}/J diverges at $T \rightarrow T_M$, showing the expected scaling with $1/M_s$. We find $\theta_{SH} \approx 7 \times 10^{-4} > 0$ [Fig. 2(e)], which is about 100 times smaller than the reported Co/Pt interfacial effect ($\theta_{SH} \sim 0.05$ in Co/Pt) [33]. θ_{SH} is independent of temperature and, in particular, does not change across T_M , which is consistent with the hypothesis of the SHE as the main source of H_{DL} .

Figure 2(d) shows the H_{FL} per current density (H_{FL}/J) at various temperatures below T_M . We cannot reliably extract H_{FL} above T_M due to increasing noise with temperature (see the Supplemental Material [30]). At a fixed temperature, H_{FL} does not change sign with reversal of the magnetization, as expected with symmetry, $\mathbf{H}_{FL} = H_{FL}\hat{\sigma}$. In addition to SOTs, the current generates an Oersted field (H_{Oe}) that is independent of M_s but has the same orientation as H_{FL} . Therefore, H_{Oe} contributes to the measured H_{FL} [see the horizontal line in Fig. 2(d)]. However, the divergence of H_{FL} as $T \rightarrow T_M$ shows that a non-Oersted torque is present. Assuming a Rashba-induced H_{FL} , it would depend on M_s with the following relationship:

$$\mu_0 H_{FL} = -\frac{2m_e}{\hbar e M_s} \alpha_R P J,$$

where m_e is the electron mass, P is the current polarization, and α_R is the Rashba parameter. This relationship matches well with the obtained variation of H_{FL} . Figure 2(f) shows the extracted $\alpha_R P$ at various temperatures. The obtained value of $\alpha_R P \approx 7 \times 10^{-33} Jm$ is independent of temperature, suggesting the presence of a significant SOT-induced H_{FL} . The existence of these SOTs in a ferrimagnetic layer without an adjacent HM suggests the presence of an internal SOC from the magnetic layer itself.

IV. CHIRAL SPIN TEXTURES AND DZYALOSHINSKII-MORIYA INTERACTION

Another phenomenon induced by SOC is the DMI, which favors chiral magnetic textures [15,34,35]. We examine the internal structure of DWs in the ferrimagnetic film using photoemission electron microscopy combined with x-ray magnetic circular dichroism (XMCD PEEM)

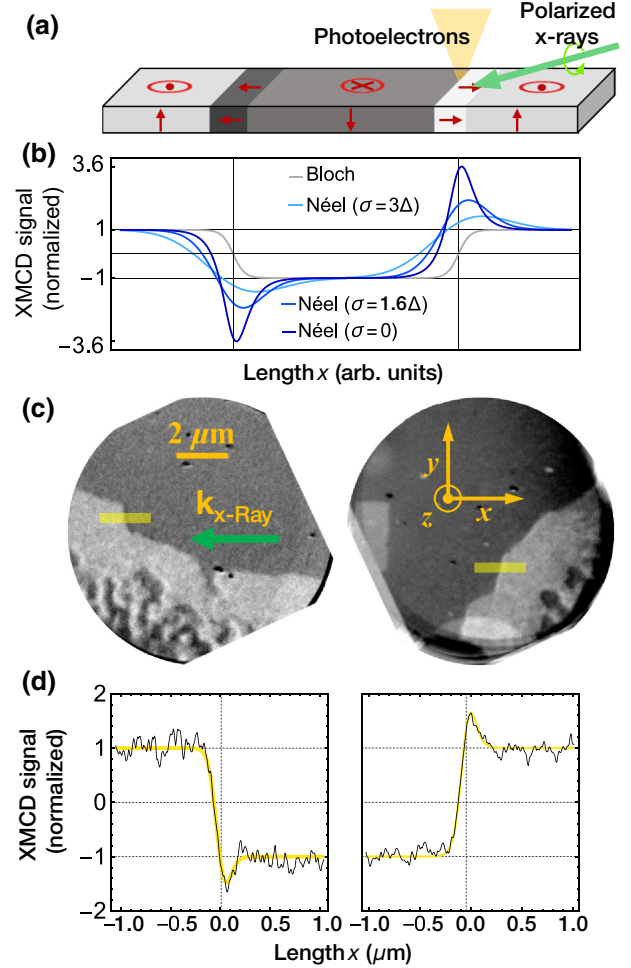


FIG. 3. (a) Schematic of the XMCD PEEM experiment, showing the magnetization profile of up-down and down-up left-handed Néel DWs and the x-ray beam with grazing incidence (16°) and perpendicular to the DW length. (b) Calculated normalized XMCD PEEM intensity profile for DWs in (a), taking into account the finite microscope resolution (r ; blue curves). Gray curve is the profile of Bloch DWs. (c) Multidomain XMCD PEEM images at the Gd $M_{4,5}$ edge (1178.7 eV). Green arrow shows the direction of the x-ray beam. Dark (bright) contrast corresponds to a down (up) magnetic domain. Analyzed DWs are in the vicinity of a region of lowered anisotropy induced by long exposure to x-rays (with small domains; in the bottom). (d) Intensity profiles (black lines) averaged over yellow regions in (c). Thick yellow line is a fit using the theoretical profile, as shown in (a), with $r = 60$ nm, which is measured on dust particles in the image.

[36]. In our experiment, the incident x-ray energy is set to the Gd $M_{4,5}$ absorption edge at a grazing angle of 16° [see Fig. 3(a)]. In XMCD, the contrast is proportional to $\hat{\mathbf{k}}_{x\text{-ray}} \cdot \hat{\mathbf{m}}$ (where $\hat{\mathbf{k}}_{x\text{-ray}}$ is the unit vector along the incident beam), resulting in 3.5 times higher in-plane contrast than that of the out-of-plane contrast. Therefore, Néel and Bloch DWs, as well as their chirality, can be distinguished by their different XMCD PEEM profiles [35], even when the DW width (Δ) is smaller than the microscope resolution (r) [see Fig. 3(b)].

Imaging is performed at $T = 230 \text{ K} < T_M$ to avoid thermal magnetization fluctuations. Figure 3(c) shows typical XMCD PEEM images of up and down domains manifested by light and dark gray contrasts, respectively (see the Supplemental Material [30] for more images). Interestingly, an intense black or white contrast appears between the domains when the DW length is perpendicular to the incident beam, while it is absent when the incident beam is along the DW length. The intense DW contrast is clearly visible on the XMCD line scans [Fig. 3(d)], as evidenced by either a peak or a dip between the dark and light gray domains. This pattern shows that the DW magnetization lies parallel or antiparallel to the x-ray beam, that is, the DW is of Néel type with left-handed chirality. To acquire the DW width and internal magnetization direction, we fit the obtained XMCD line scans with the expected profile convoluted with a Gaussian function to account for the microscope's resolution. By fitting several line scans of DWs with different orientations, keeping the azimuthal angle (φ) and Δ as free parameters [Fig. 3(d)], we obtain $\varphi = (180 \pm 10)^\circ$ (left-handed Néel) and $\Delta = (20 \pm 10) \text{ nm}$. As the ferrimagnetic film is not interfaced with any HM,

these chiral Néel DWs clearly indicate the existence of DMI in the volume of the film.

To quantify the magnitude and sign of the DMI, we perform spin-wave (SW) spectroscopy experiments using the Brillouin light-scattering (BLS) technique in Damon-Eshbach geometry [see inset in Fig. 4(a)] at room temperature (293 K) [37]. This method measures Stokes (f_S) and anti-Stokes (f_{AS}) resonance frequencies, which correspond to counterpropagating SWs [Fig. 4(a)]. Due to the DMI, they have different frequencies. The variation of this difference, $\Delta f = f_{AS} - f_S$, with the incident wave vector, k_{SW} , is directly proportional to the DMI parameter, D : $\Delta f = -(2\gamma/\pi M_s) D k_{SW}$, with γ being the gyromagnetic ratio of the alloy [37–42] (see the Supplemental Material [30]).

A typical BLS spectrum for the same sample is shown in Fig. 4(a) and the dependency of Δf with k_{SW} is shown in Fig. 4(b). A value of $D = (-8.4 \pm 2.5) \mu\text{J}/\text{m}^2$ is obtained from Δf vs k_{SW} . This DMI magnitude is much smaller than those of Ta/Co and Pt/Co systems [38].

To understand the stabilization of Néel DWs with such a low D , we must consider the critical DMI [$D_C = (4/\pi)\Delta K \approx (2\ln 2/\pi^2)t \mu_0 M_S^2$] required to form a Néel DW in thin films [1]. Due to the low M_S of this system, D is indeed about ~ 4 times larger than the estimated D_C at the temperature of the PEEM experiments ($D_C \approx 2.3 \mu\text{J}/\text{m}^2$). This shows that a small DMI can still be dominant in low- M_S systems. Therefore, the extracted D favors the left-handed ($D < 0$) Néel DW structure ($|D| > D_C$), as observed in the PEEM experiments.

Further insights into the origin of these effects are obtained by comparing θ_{SH} and D of this film with a control sample with a Pt capping layer [Si/SiO_x/Gd-Fe-Co (5 nm)/Pt(7 nm)], for which the usual interfacial effects should be present. We find a median value of $\theta_{SH} = -0.12$ in the Gd-Fe-Co/Pt sample (see the Supplemental Material [30]), with an opposite sign to that of Gd-Fe-Co/Al. Furthermore, the DMI parameter D for the Pt-capped control sample is determined to be $D = (27.2 \pm 0.2) \mu\text{J}/\text{m}^2$ [Fig. 4(c)]. The sign of D is the same as that reported for the Co/Pt interface [38] and is opposite to that of the Gd-Fe-Co/Al sample. The magnitude of D agrees with the naïve expectation that Gd-Fe-Co/Pt, containing only 10% Co, should show about 10% of the DMI of pure Co/Pt interfaces [38]. These findings show that the DMI and SOTs in the control Gd-Fe-Co/Pt sample are dominated by interfacial effects, unlike what was found for the DMI in another study [25].

V. THICKNESS DEPENDENCE OF DMI AND SOTs

To investigate the origin of the DMI and SOTs in Gd-Fe-Co/Al, we study samples with different Gd-Fe-Co thicknesses. The measured DMI values for 4-, 5-, 6-, and 8-nm-thick samples are shown in Fig. 5(a)

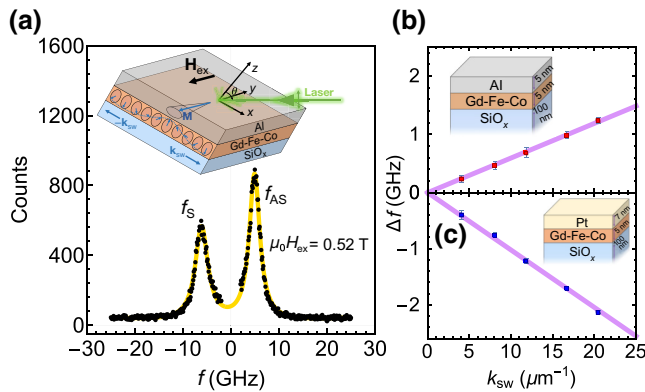


FIG. 4. (a) BLS spectrum of SiO_x/Gd-Fe-Co/Al obtained with a laser wavelength of 532 nm at 293 K under an in-plane magnetic field, $\mu_0 H_{ex} = 0.52 \text{ T}$, and at beam incidence angle (θ) of 60° (corresponding to $|k_{SW}| = 20.46 \mu\text{m}^{-1}$). Yellow lines are Lorentzian fits. Inset shows measurement geometry. DMI-induced frequency shifts (Δf) of nonreciprocal SWs vs wave-vector magnitudes $|k_{SW}|$ for (b) Al-covered (red) and (c) Pt-covered (blue) films. Thick lines are linear fits. Both samples are measured at $T < T_M$.

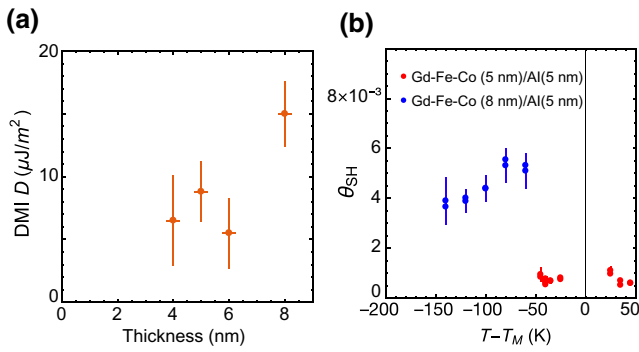


FIG. 5. (a) DMI values measured by BLS as a function of Gd-Fe-Co thickness [in Gd-Fe-Co(t nm)/Al(5 nm)] (b) Spin Hall angle as a function of temperature for 5 nm Gd-Fe-Co/Al (red) and 8 nm Gd-Fe-Co/Al samples (blue).

and they do not show a variation with thickness. The interfacial mechanism would exhibit $1/t$ variation of the DMI parameter, as found in Pt/Co samples [38], where t is the thickness of the magnetic layer. Therefore, these results suggest that the DMI cannot be produced by a pure interfacial mechanism.

Furthermore, we measure SOTs in the Gd-Fe-Co (8 nm)/Al(5 nm) sample, and a fivefold increase in SOTs is observed [Fig. 5(b)], which further excludes the possibility of a dominating interfacial SOC mechanism and suggests the bulk origin of the DMI and SOTs. However, the interfacial mechanism dominates over bulk contributions when Gd-Fe-Co is interfaced with a strong SOC material, as we show in Gd-Fe-Co/Pt samples.

VI. COMPOSITION PROFILE

The presence of the DMI and SOT in thin films without a HM adjacent layer is far from trivial and suggests that they originate from the intrinsic properties of the magnetic film. These phenomena require broken inversion symmetry. To investigate the origin of the inversion asymmetry in the film, electron energy-loss spectroscopy (EELS) studies are performed with scanning transmission electron microscopy (STEM) of cross-section views [24,25,27,43]. Typical high-angle annular dark-field (HAADF) and bright-field (BF) STEM images of the SiO_x/Gd-Fe-Co/Al film are shown in Figs. 6(a) and 6(b), respectively. The Gd-Fe-Co layer can be clearly identified by higher contrast in the HAADF image, while both SiO_x and AlO_x layers are distinguishable by their lower contrasts. The ferrimagnetic layer presents a homogeneous thickness of about (5.2 ± 0.4) nm, with defined bottom and top interfaces running along the observed film (see Fig. S16 within the Supplemental Material [30]). The BF image presents clear amorphous contrast in the Gd-Fe-Co alloy across the total thin-film thickness, which rules out any noncentrosymmetric crystal structure.

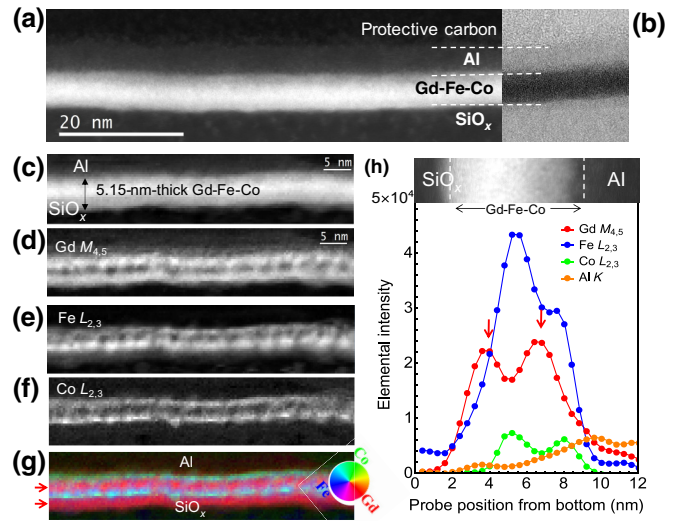


FIG. 6. (a) HAADF and (b) BF STEM images of the SiO_x/Gd-Fe-Co/Al cross section. (c) HAADF intensity map of the probed area with corresponding elemental maps extracted at (d) Gd $M_{4,5}$, (e) Fe $L_{2,3}$, and (f) Co $L_{2,3}$ edges. (g) Superimposed “false-color” map of Gd (red), Fe (blue), and Co (green). (h) Laterally integrated line profiles over a length of 12 nm of Gd $M_{4,5}$ (red), Co $L_{2,3}$ (green), Fe $L_{2,3}$ (blue), and Al K (orange) intensities along the film thickness.

Next, we reveal by EELS a nonuniform elemental distribution in the Gd-Fe-Co layer, in agreement with our previous observations in other rare-earth–transition-metal films [27]. The elemental maps and profiles [Figs. 6(c)–6(e)] clearly evidence an anticorrelated spatial distribution of Gd [Fig. 6(d)] and $3d$ TM elements [Fe in Fig. 6(e) and Co in Fig. 6(f)] throughout the ferrimagnetic layer (see Fig. S17 within the Supplemental Material [30]). This peculiar elemental dissociation is present along the whole amorphous film, while its depth distribution is nanostructured as follows: a first Gd-rich layer of about 1.6 nm at the bottom interface, followed by a first Fe-Co-rich intermediate layer of about 1.2 nm, then a second Gd-rich layer of about 1.2 nm, and finally a thin Fe-Co-rich layer of about 1 nm at the top interface. Furthermore, while the Gd-rich layers appear homogeneous along the entire film [marked by red arrows in Figs. 6(g) and 6(h)], the Fe-Co-rich layers form aggregated nanostructures separated regularly by (2.8 ± 0.4) nm. These findings highlight a nanostructure alternating between Gd- and Fe-Co-rich sublayers, in contrast with previous work reported for thicker Gd-Fe-Co films [25]. A similar structure is found in the Pt-capped sample (see the Supplemental Material [30]). This elemental inhomogeneity breaks the spatial-inversion symmetry and enables the emergence of net SOC effects inside the Gd-Fe-Co layer. A similar dependence with composition gradient in heavy metals was reported for a Fe-Pt film [44],

although in Tb-Co the effects were found to be independent of the composition gradient [45].

VII. CONCLUSION

We measure a net SOT, a significant DMI, and chiral Néel DWs in single thin ferrimagnetic films without any HM interface. This provides threefold experimental evidence of an internal SOC and inversion asymmetry. The fact that the DMI and SOT do not decrease with thickness is further confirmation of a dominating internal SOC mechanism. We attribute the SOC to the electronic hybridization of RE $5d$ and TM $3d$ electrons. The source of asymmetry is elemental inhomogeneity along the depth. The internal DMI and SOTs superimpose with interfacial effects and, therefore, should not be overlooked in the analysis of stability and dynamics of magnetic textures. Moreover, these internal effects can be engineered by tuning the composition profile along the film thickness. Our findings not only provide insights into the physics of ferrimagnetic alloys but also open additional paths to design and engineer advanced materials for ultrafast spintronics applications.

ACKNOWLEDGMENTS

We are very thankful to Stanislas Rohart for fruitful discussions, Richard Mattana for the SQUID measurements of M_S , and Nathalie Brun for assistance with the analysis of STEM data. S.K. and E.H. acknowledge a public grant overseen by the ANR as part of the “Investissements d’Avenir” program (Labex NanoSaclay, Grant No. ANR-10-LABX-0035) for the FEMINIST project and traveling grants. S.K. acknowledges a public grant from PIAF (Grant No. ANR-17-CE09-0030). Transport measurements are supported by the Université Paris-Sud Grant MRM PMP. We acknowledge funding from the ANR under the “Investissements d’Avenir” program TEMPOS (Grant No. ANR-10_EQPX-50) for focused ion beam access.

Note added.—Recently, similar internal SOTs were also reported in a ferrimagnet [46] and in ferromagnetic Co-Pt [47], which further supports the explanation based on an internal mechanism.

-
- [1] A. Thiaville, S. Rohart, É. Jué, V. Cros, and A. Fert, Dynamics of dzyaloshinskii domain walls in ultrathin magnetic films, *EPL* **100**, 577002 (2012).
 - [2] S. Emori, U. Bauer, S.-M. Ahn, E. Martinez, and G. S. D. Beach, Current-Driven dynamics of chiral ferromagnetic domain walls, *Nat. Mater.* **12**, 611 (2013).
 - [3] K.-S. Ryu, L. Thomas, S.-H. Yang, and S. Parkin, Chiral spin torque at magnetic domain walls, *Nat. Nanotechnol.* **8**, 527 (2013).

- [4] A. Soumyanarayanan, N. Reyren, A. Fert, and C. Panagopoulos, Emergent phenomena induced by spin-orbit coupling at surfaces and interfaces, *Nature* **539**, 509 (2016).
- [5] M. I. Dyakonov and V. I. Perel, Current-induced spin orientation of electrons in semiconductors, *Phys. Lett. A* **35**, 459 (1971).
- [6] C. Stamm, C. Murer, M. Berritta, J. Feng, M. Gabureac, P. M. Oppeneer, and P. Gambardella, Magneto-optical Detection of the Spin Hall Effect in Pt and W Thin Films, *Phys. Rev. Lett.* **119**, 087203 (2017).
- [7] J. C. R. Sánchez, L. Vila, G. Desfonds, S. Gambarelli, J. P. Attané, J. M. De Teresa, C. Magén, and A. Fert, Spin-to-Charge conversion using rashba coupling at the interface between non-magnetic materials, *Nat. Commun.* **4**, 2944 (2013).
- [8] A. Manchon and A. Belabbes, *Spin-Orbitronics at Transition Metal Interfaces*, 1st ed., Vol. 68 (Cambridge, MA, USA, 2017).
- [9] J. Kim, J. Sinha, M. Hayashi, M. Yamanouchi, S. Fukami, T. Suzuki, S. Mitani, and H. Ohno, Layer thickness dependence of the current-induced effective field vector in Ta[CoFeB]/MgO, *Nat. Mater.* **12**, 240 (2013).
- [10] L. Liu, C. F. Pai, Y. Li, H. W. Tseng, D. C. Ralph, and R. A. Buhrman, Spin-torque switching with the giant spin Hall effect of tantalum, *Science* (80-) **336**, 555 (2012).
- [11] K. Garello, I. M. Miron, C. O. Avci, F. Freimuth, Y. Mokrousov, S. Blügel, S. Auffret, O. Boulle, G. Gaudin, and P. Gambardella, Symmetry and magnitude of spin-orbit torques in ferromagnetic heterostructures, *Nat. Nanotechnol.* **8**, 587 (2013).
- [12] S. Emori, T. Nan, A. M. Belkessam, X. Wang, A. D. Matyushov, C. J. Babroski, Y. Gao, H. Lin, and N. X. Sun, Interfacial spin-orbit torque without bulk spin-orbit coupling, *Phys. Rev. B* **93**, 1 (2016).
- [13] W. Wang, T. Wang, V. P. Amin, Y. Wang, A. Radhakrishnan, A. Davidson, S. R. Allen, T. J. Silva, H. Ohldag, D. Balzar, B. L. Zink, P. M. Haney, J. Q. Xiao, D. G. Cahill, V. O. Lorenz, and X. Fan, Anomalous spin-orbit torques in magnetic single-layer films, *Nat. Nanotechnol.* **14**, 819 (2019).
- [14] J. Sampaio, V. Cros, S. Rohart, A. Thiaville, and A. Fert, Nucleation, stability and current-induced motion of isolated magnetic skyrmions in nanostructures, *Nat. Nanotechnol.* **8**, 839 (2013).
- [15] L. Caretta, M. Mann, F. Büttner, K. Ueda, B. Pfau, C. M. Günther, P. Helsing, A. Churikova, C. Klose, M. Schneider, D. Engel, C. Marcus, D. Bono, K. Bagschik, S. Eisebitt, and G. S. D. Beach, Fast current-driven domain walls and small skyrmions in a compensated ferrimagnet, *Nat. Nanotechnol.* **13**, 1154 (2018).
- [16] E. Haltz, J. Sampaio, S. Krishnia, L. Berges, R. Weil, and A. Mougin, Measurement of the tilt of a moving domain wall shows precession-free dynamics in compensated ferrimagnets, *Sci. Rep.* **10**, 16292 (2020).
- [17] E. Haltz, S. Krishnia, L. Berges, A. Mougin, and J. Sampaio, Domain wall dynamics in antiferromagnetically coupled double-lattice systems, *Phys. Rev. B* **103**, 014444 (2021).
- [18] M. S. S. Brooks, L. Nordstrom, and B. Johansson, 3d-5d band magnetism in rare earth-transition metal

- intermetallics: Total and partial magnetic moments of the RFe_2 ($R = \text{Gd-Yb}$) laves phase compounds, *J. Phys. Condens. Matter* **3**, 2357 (1991).
- [19] D. Coffey, J. L. Diez-Ferrer, D. Serrate, M. Ciria, C. D. La Fuente, and J. I. Arnaudás, Antiferromagnetic spin coupling between rare earth adatoms and iron Islands probed by spin-polarized tunneling, *Sci. Rep.* **5**, 1 (2015).
- [20] M. A. Laguna-Marco, J. Chaboy, and C. Piquer, Experimental determination of the R(5d)-T(3d) hybridization in rare-earth intermetallics, *Phys. Rev. B* **77**, 125132 (2008).
- [21] H. Jang, B. Y. Kang, B. K. Cho, M. Hashimoto, D. Lu, C. A. Burns, C. C. Kao, and J. S. Lee, Observation of Orbital Order in the Half-Filled 4f Gd Compound, *Phys. Rev. Lett.* **117**, 1 (2016).
- [22] S. Schulz, I. A. Nechaev, M. Güttler, G. Poelchen, A. Generalov, S. Danzenbächer, A. Chikina, S. Seiro, K. Kliemt, A. Y. Vyazovskaya, T. K. Kim, P. Dudin, E. V. Chulkov, C. Laubschat, E. E. Krasovskii, C. Geibel, C. Krellner, K. Kummer, and D. V. Vyalikh, Emerging 2D-ferromagnetism and strong spin-orbit coupling at the surface of valence-fluctuating EuIr_2Si_2 , *Npj Quantum Mater.* **4**, 26 (2019).
- [23] S. Véléz, J. Schaab, M. S. Wörmle, M. Müller, E. Gradauskaite, P. Welter, C. Gutgsell, C. Nistor, C. L. Degen, M. Trassin, M. Fiebig, and P. Gambardella, High-speed domain wall racetracks in a magnetic insulator, *Nat. Commun.* **10**, 1 (2019).
- [24] L. Caretta, E. Rosenberg, F. Büttner, T. Fakhrul, P. Gargiani, M. Valvidares, Z. Chen, P. Reddy, D. A. Muller, C. A. Ross, and G. S. D. Beach, Interfacial Dzyaloshinskii-Moriya interaction arising from rare-earth orbital magnetism in insulating magnetic oxides, *Nat. Commun.* **11**, 1 (2020).
- [25] D. H. Kim, *et al.*, Bulk Dzyaloshinskii-Moriya interaction in amorphous ferrimagnetic alloys, *Nat. Mater.* **18**, 685 (2019).
- [26] J. Yu, D. Bang, R. Mishra, R. Ramaswamy, J. H. Oh, H. J. Park, Y. Jeong, P. Van Thach, D. K. Lee, G. Go, S. W. Lee, Y. Wang, S. Shi, X. Qiu, H. Awano, K. J. Lee, and H. Yang, Long spin coherence length and bulk-like spin-orbit torque in ferrimagnetic multilayers, *Nat. Mater.* **18**, 29 (2019).
- [27] E. Haltz, R. Weil, J. Sampaio, A. Pointillon, O. Rousseau, K. March, N. Brun, Z. Li, E. Briand, C. Bachelet, Y. Dumont, and A. Mougin, Deviations from bulk behavior in TbFe(Co) thin films: Interfaces contribution in the biased composition, *Phys. Rev. Mater.* **2**, 104410 (2018).
- [28] P. Hansen, C. Clausen, G. Much, M. Rosenkranz, and K. Witter, Magnetic and magneto-optical properties of rare-earth transition-metal alloys containing Gd, Tb, Fe, Co, *J. Appl. Phys.* **66**, 756 (1989).
- [29] R. Wood, Exact solution for a Stoner-Wohlfarth particle in an applied field and a new approximation for the energy barrier, *IEEE Trans. Magn.* **45**, 100 (2009).
- [30] See the Supplemental Material at <http://link.aps.org/supplemental/10.1103/PhysRevApplied.16.024040> for additional characterization, measurements, examples of raw data, and details on the calculations of the torque magnitude.
- [31] H. Wu, Y. Xu, P. Deng, Q. Pan, S. A. Razavi, K. Wong, L. Huang, B. Dai, Q. Shao, G. Yu, X. Han, J. C. Rojas-Sánchez, S. Mangin, and K. L. Wang, Spin-orbit torque switching of a nearly compensated ferrimagnet by topological surface states, *Adv. Mater.* **31**(35), 1901681 (2019).
- [32] A. V. Khvalkovskiy, V. Cros, D. Apalkov, V. Nikitin, M. Krounbi, K. A. Zvezdin, A. Anane, J. Grollier, and A. Fert, Matching domain-wall configuration and spin-orbit torques for efficient domain-wall motion, *Phys. Rev. B - Condens. Matter Mater. Phys.* **87**, 020402 (2013).
- [33] J. C. Rojas-Sánchez, N. Reyren, P. Laczkowski, W. Savero, J. P. Attané, C. Deranlot, M. Jamet, J. M. George, L. Vila, and H. Jaffrès, Spin Pumping and Inverse Spin Hall Effect in Platinum: The Essential Role of Spin-Memory Loss at Metallic Interfaces, *Phys. Rev. Lett.* **112**, 106602 (2014).
- [34] R. Streubel, C. H. Lambert, N. Kent, P. Ercius, A. T. N'Diaye, C. Ophus, S. Salahuddin, and P. Fischer, Experimental evidence of chiral ferrimagnetism in amorphous GdCo films, *Adv. Mater.* **30**(27), 1800199 (2018).
- [35] O. Boulle, *et al.*, Room-temperature chiral magnetic skyrmions in ultrathin magnetic nanostructures, *Nat. Nanotechnol.* **11**, 449 (2016).
- [36] L. Aballe, M. Foerster, E. Pellegrin, J. Nicolas, and S. Ferrer, The ALBA spectroscopic LEEM-PEEM experimental station: Layout and performance, *J. Synchrotron Radiat.* **22**, 745 (2015).
- [37] K. Di, V. L. Zhang, H. S. Lim, S. C. Ng, M. H. Kuok, J. Yu, J. Yoon, X. Qiu, and H. Yang, Direct Observation of the Dzyaloshinskii-Moriya Interaction in a Pt/Co/Ni Film, *Phys. Rev. Lett.* **114**, 047201 (2015).
- [38] M. Belmeguenai, J. P. Adam, Y. Roussigné, S. Eimer, T. Devolder, J. Von Kim, S. M. Cherif, A. Stashkevich, and A. Thiaville, Interfacial Dzyaloshinskii-Moriya interaction in perpendicularly magnetized Pt/Co/AlOx ultrathin films measured by Brillouin light spectroscopy, *Phys. Rev. B - Condens. Matter Mater. Phys.* **91**, 180405(R) (2015).
- [39] O. Gladii, M. Haidar, Y. Henry, M. Kostylev, and M. Bailleul, Frequency nonreciprocity of surface spin wave in permalloy thin films, *Phys. Rev. B* **93**, 054430 (2016).
- [40] Y. Quessab, J. W. Xu, C. T. Ma, W. Zhou, G. A. Riley, J. M. Shaw, H. T. Nembach, S. J. Poon, and A. D. Kent, Tuning interfacial Dzyaloshinskii-Moriya interactions in thin amorphous ferrimagnetic alloys, *Sci. Rep.* **10**, 7447 (2020).
- [41] J. H. Moon, S. M. Seo, K. J. Lee, K. W. Kim, J. Ryu, H. W. Lee, R. D. McMichael, and M. D. Stiles, Spin-wave propagation in the presence of interfacial Dzyaloshinskii-Moriya interaction, *Phys. Rev. B - Condens. Matter Mater. Phys.* **88**, 184404 (2013).
- [42] D. Raasch, J. Reck, C. Mathieu, and B. Hillebrands, Exchange stiffness constant and wall energy density of amorphous GdTb-FeCo thin films, *J. Appl. Phys.* **76**, 1145 (1994).
- [43] K. Davob, A. Foi, V. Katkovnik, and K. Egiazarian, Image denoising by sparse 3-D transform-domain collaborative filtering, *IEEE Trans. Image Process.* **16**, 1 (2007).
- [44] L. Liu, J. Yu, R. González-Hernández, C. Li, J. Deng, W. Lin, C. Zhou, T. Zhou, J. Zhou, H. Wang, R. Guo, H. Y. Yoong, G. M. Chow, X. Han, B. Dupé, J. Železný, J. Sinova, and J. Chen, Electrical switching of perpendicular magnetization in a single ferromagnetic layer, *Phys. Rev. B* **101**, 220402 (2020).
- [45] J. W. Lee, J. Y. Park, J. M. Yuk, and B. G. Park, Spin-orbit Torque in a Perpendicularly Magnetized Ferrimagnetic

- Tb – Co Single Layer, [Phys. Rev. Appl. **13**, 044030 \(2020\)](#).
- [46] D. Céspedes-Berrocal, H. Damas, S. Petit-Watelot, D. Macariello, P. Tang, A. Arriola-Córdova, P. Vallobra, Y. Xu, J. L. Bello, E. Martin, S. Migot, J. Ghanbaja, S. Zhang, M. Hehn, S. Mangin, C. Panagopoulos, V. Cros, A. Fert, and J. C. Rojas-Sánchez, Current-induced spin torques on single GdFeCo magnetic layers, [Adv. Mater. **33**, 2007047 \(2021\)](#).
- [47] L. Zhu, X. S. Zhang, D. A. Muller, D. C. Ralph, and R. A. Buhrman, Observation of strong bulk damping-like spin-orbit torque in chemically disordered ferromagnetic single layers, [Adv. Funct. Mater. **30**\(48\), 2005201 \(2020\)](#).